HHS Public Access

Author manuscript

Ultrasonics. Author manuscript; available in PMC 2017 August 01.

Published in final edited form as:

Ultrasonics. 2016 August ; 70: 123–135. doi:10.1016/j.ultras.2016.04.022.

Adaptive windowing in contrast-enhanced intravascular ultrasound imaging

Brooks D. Lindsey[1], **K. Heath Martin**[1], **Xiaoning Jiang**[2,1], and **Paul A. Dayton**[1,3]

[1]Joint Department of Biomedical Engineering, University of North Carolina at Chapel Hill and North Carolina State University, CB7575, Chapel Hill, NC 27599

[2]Department of Mechanical and Aerospace Engineering, North Carolina State University, 911 Oval Drive, 3282 Engineering Building III, Campus Box 7910, North Carolina State University, Raleigh, NC

[3]Biomedical Research Imaging Center, University of North Carolina at Chapel Hill, Marsico Hall, Chapel Hill, NC 27599

Abstract

Intravascular ultrasound (IVUS) is one of the most commonly-used interventional imaging techniques and has seen recent innovations which attempt to characterize the risk posed by atherosclerotic plaques. One such development is the use of microbubble contrast agents to image *vasa vasorum*, fine vessels which supply oxygen and nutrients to the walls of coronary arteries and typically have diameters less than 200 μm. The degree of *vasa vasorum* neovascularization within plaques is positively correlated with plaque vulnerability. Having recently presented a prototype dual-frequency transducer for contrast agent-specific intravascular imaging, here we describe signal processing approaches based on minimum variance (MV) beamforming and the phase coherence factor (PCF) for improving the spatial resolution and contrast-to-tissue ratio (CTR) in IVUS imaging. These approaches are examined through simulations, phantom studies, *ex vivo* studies in porcine arteries, and *in vivo* studies in chicken embryos. In phantom studies, PCF processing improved CTR by a mean of 4.2 dB, while combined MV and PCF processing improved spatial resolution by 41.7%. Improvements of 2.2 dB in CTR and 37.2% in resolution were observed *in vivo*. Applying these processing strategies can enhance image quality in conventional B-mode IVUS or in contrast-enhanced IVUS, where signal-to-noise ratio is relatively low and resolution is at a premium.

Keywords

intravascular ultrasound; contrast-enhanced ultrasound; adaptive beamforming; phase coherence factor; high frequency ultrasound; superharmonic

Corresponding author: Brooks Lindsey, Ph.D., Postdoctoral Research Fellow, UNC-NCSU Joint Department of Biomedical Engineering, 152 MacNider Hall, CB 7575, Chapel Hill, NC, 27599, phone: (217) 621 3758, fax: (919) 843 9520, brooks.lindsey@unc.edu.

1. Introduction

According to the World Health Organization, ischemic heart disease was the leading cause of death globally in 2012 [1]. In assessing ischemic heart disease, intravascular ultrasound (IVUS) is the imaging modality of choice because it allows direct visualization of stenotic coronary arteries and accumulated plaques with minimal invasiveness. Conventional grayscale (B-mode) IVUS imaging is useful for determining plaque extent and morphology [2], for guiding percutaneous coronary interventions (PCI), and for assessment of stent placement in follow-up imaging [3]. However, grayscale IVUS cannot reliably identify vulnerable plaques, i.e. those which are likely to rupture and produce ensuing ischemic cardiac events such as myocardial infarction [4, 5].

Several strategies for assessing plaque vulnerability based on spectral content of radiofrequency IVUS data have recently been evaluated in the clinical setting [3, 6–8]. However, these emerging techniques have yet to demonstrate the diagnostic power necessary for widespread clinical adoption. In addition to imaging strategies based on ultrasound elastography [9], optical coherence tomography (OCT) [10], or photoacoustics [11, 12], several promising techniques for contrast-enhanced IVUS imaging have been presented, including approaches which utilize echoes from microbubble contrast agents within intra-plaque vessels at subharmonic [13, 14], second harmonic [15, 16], or ultraharmonic frequencies [14, 17], and an approach using radial modulation imaging with a clinical transducer [18].

Specifically, contrast-enhanced intravascular ultrasound imaging provides information on plaque morphology by imaging the *vasa vasorum*—blood vessels which supply the arterial walls. Intra-plaque hemorrhage from defective *vasa vasorum* is believed to contribute to the development of vulnerable plaques [5]. The *vasa vasorum* itself may be divided into two structures, the primary *vasa vasorum*, which supplies vessel walls directly (mean diameter ~160 μm), and the secondary *vasa vasorum* (mean diameter ~70 μm), which in turn supplies the primary *vasa vasorum* [19]. These diameters represent resolution benchmarks for *vasa vasorum* imaging.

Despite the demonstrated promise of contrast-enhanced IVUS, there are several technical challenges which have prevented this imaging approach from realizing its full clinical potential. First, the resonance frequencies of commercial microbubble contrast agents are typically <10 MHz [20], while transducers used in coronary IVUS typically operate at frequencies >20 MHz, making them poor excitation sources for microbubbles. While this may be partially addressed through aforementioned approaches such as radial modulation, subharmonic, or second harmonic imaging, bandwidth limitations in commercial IVUS transducers generally result in reductions in either transmit pressure, receive sensitivity, or both. Forming images from subharmonic echoes leads to poor resolution which is undesirable for the goal of imaging the fine vasculature of the *vasa vasorum*. In small vessels containing relatively few microbubbles, sensitivity is also at a premium, accentuating losses due to operating off-resonance when transmitting or receiving.

We have recently developed a prototype dual-frequency transducer which allows for excitation of microbubbles at 6.5 MHz and reception of superharmonic echoes at 30 MHz with a −6 dB fractional bandwidth of 59% [21, 22]. Several other dual-frequency transducers for microbubble contrast agent imaging have recently been fabricated by our group as well as others [23–27]. Forming images from echoes near 30 MHz produces high resolution images of microbubbles. Because the amplitude of tissue harmonic echoes is low relative to microbubble echoes at these frequencies, this imaging scenario permits acquisition of high contrast-to-tissue ratio (CTR) images of vasculature alone [28, 29]. This work in assessing *vasa vasorum* with catheter-based transducers builds on previous studies which have demonstrated the ability to quantify microvascular tortuosity in vessels on the order of ~200 μm [30, 31] using a large, external dual-frequency transducer.

In recent years, the application of Capon (minimum variance) beamforming to ultrasound imaging has received great attention due to its ability to offer improved resolution by adaptively steering toward on-axis scatterers [32–34]. More recently, several groups have reported improvements to classical minimum variance beamforming when applied to ultrasound imaging by reducing computational complexity or improving robustness [35, 36], applying coherence factor weightings [37], or implementing in the frequency domain [38]. In general, these authors report increased spatial resolution, increased contrast, and decreased contrast-to-noise ratio (CNR) in B-mode ultrasound images as a result of applying minimum variance beamforming techniques [32–38].

An alternative adaptive approach for the improvement of spatial resolution and image contrast is the application of the phase coherence factor (PCF), which is computed using channel data but applied after beamforming. Camacho et al. first presented the phase coherence factor as an approach for decreasing sidelobe contributions in ultrasound images, with concomitant improvements in lateral resolution and beamsummed signal-to-noise ratio (SNR) [39]. More recently, Hasegawa and Kanai demonstrated the application of the phase coherence factor to increase resolution in echocardiography while using sub-aperture beamforming to reduce suppression of echoes from diffuse, speckle-producing targets, such as those in the cardiac wall which are essential for diagnosis [40].

Adaptive beamforming and adaptive imaging remain unexplored in the context of contrast-enhanced ultrasound imaging, despite the fact that microbubbles represent an ideal target for a beamformer having high point target resolution. Additionally, when a dual-frequency contrast imaging approach is used, echoes originating from tissue scatterers will be minimized due to the low energy generated by tissue relative to microbubbles at high frequencies [28]. This may mitigate the reduced performance of minimum variance ultrasound imaging that occurs when there is a high degree of correlation between signals acquired on neighboring elements.

In this work, we investigate approaches for improving the CTR and spatial resolution in contrast-enhanced intravascular ultrasound imaging using both minimum variance beamforming (MV) and the phase coherence factor (PCF). These techniques are applied to prototype dual-frequency IVUS ultrasound transducers [21], which provide high-contrast, high-resolution images in an 8 French form factor. It should be noted that the experiments

presented in this work represent a scenario in which the majority of microbubbles in the main artery have been cleared by saline flush in order to image microbubbles in the *vasa vasorum*, an approach which is analogous to that described for intravascular optical coherence tomography where saline boluses are commonly used during percutaneous interventions to clear red blood cells for imaging vessel endothelium [41]. To our knowledge, this is the first application of adaptive beamforming to either contrast-enhanced ultrasound or intravascular ultrasound imaging.

2. Background

2.1 Imaging system

The transducer used in this work has previously been described by Ma et al. [21, 26]; its characteristics are given in Table 1. Briefly, this transducer utilizes a single low frequency element to transmit signals which induce nonlinear microbubble oscillations and a separate high frequency element to receive only the higher harmonics produced by microbubbles (Figure 1). Both elements are composed of lead magnesium niobate-lead titanate (PMN-PT) single crystal in a stacked configuration such that the high frequency element is positioned in front of a larger low frequency element. The transmitting element had an aperture measuring 0.6 mm by 3 mm (lateral by elevational) while the receive element had an aperture of 0.6 mm by 0.5 mm. This transducer was mounted on the end of a hypodermic needle and the needle hub was attached to the drive shaft of a stepper motor. Motor rotation and data acquisition were controlled through LabView (National Instruments, Austin, TX) via a microcontroller (Arduino UNO, Torino, Italy) running a custom program. The stepper motor and its electronics were mounted on a computer-controlled three-axis motion stage (Newport, Irvine, CA) to allow automated pullback for acquisition of three-dimensional imaging data. At each step along the pullback direction, the transducer was rotated through 360° for a total of 400 acquisitions (0.9° step size). For this prototype system, approximately 2 seconds were required to acquire each image slice (a full 360° rotation).

2.2 Minimum variance beamforming

Ultrasound beamforming consists of applying complex weights to an acoustic wave field which has been spatially sampled in the lateral direction by a discrete number of transducer elements and in the axial direction by a discrete number of samples. In conventional (delay-and-sum) beamforming, spatiotemporal filtering is achieved by applying a data-independent amplitude weighting or apodization (for example, a rectangular or Gaussian window) to acquired data in the lateral direction, with delays providing focusing to individual points in the field. Alternatively, amplitude weightings may be computed which depend on the acquired sampled data, thus adaptively forming a beamsum.

While adaptive processing techniques are typically utilized for array configurations, transmitting and receiving from the same element at successive locations produces received signals containing the same information when a small step size is maintained and focusing delays are applied. For the parameters used in this study, from one step to the next, the percent overlap is 97% for the low frequency beam and 62% for the high frequency beam for a step size of 0.9° at a depth of 0.5 mm using one-way beams simulated in Field II. While

this overlap is relatively high for B-mode IVUS imaging, due to microbubble motion, differences in microbubble size, and because superharmonic imaging of microbubble contrast agents is at least partially destructive in nature, populations of microbubbles are likely to produce different signals from one pulse to the next, which would be expected to yield significantly reduced correlation in dual-frequency IVUS relative to B-mode IVUS. However, previous studies indicate that 1) lower amplitude superharmonic signals may be produced without microbubble destruction [42], and 2) superharmonic signals produced by microbubbles exhibit partial correlation across short spatial distances [28]. Thus while the performance of the signal processing techniques presented here would be expected to exhibit less improvement and greater variation for superharmonic imaging of microbubbles than for B-mode IVUS, some improvement can still be expected due to this microbubble partial coherence, which has also been reported by others [43].

In the case of mechanically-rotated IVUS, the received data matrix **X** is an [$m \times n$] matrix containing n axial samples at each of m acquisition angles. In minimum variance beamforming, the [$m \times 1$] weight vector **w** is defined as:

$$\mathbf{w}=\arg\min_{\mathbf{w}} \mathbf{w}^T\mathbf{R}\mathbf{w} \quad (1)$$

$$\text{subject to } \mathbf{w}^T\mathbf{a}=1, \quad (2)$$

where **a** is the steering vector, in this case an $m \times 1$ vector of ones because the data has already been delayed. Receive beamforming delays are computed according to the equation:

$$\tau_m(r_p)=\frac{\|r_{Tx}-r_p\|+\|r_{Rx}-r_p\|}{c}, \quad (3)$$

where r_p is the point in the field (x_p, z_p), r_{Tx} and r_{Rx} are the coordinates of the transmit and receiving elements, and c is the speed of sound. In this work, sampling frequency f_s = 100 MHz, yielding a delay resolution of 10 ns. The turning radius is 0.45 mm.

The solution to the constrained optimization problem posed by Equations 1 and 2 is:

$$\mathbf{w}=\frac{\mathbf{R}^{-1}\mathbf{a}}{\mathbf{a}^T\mathbf{R}^{-1}\mathbf{a}} \quad [44], \quad (4)$$

where **R** is the [$m \times m$] sample covariance matrix:

$$\mathbf{R}=\mathbf{X}\mathbf{X}^T \quad (5)$$

and **a** is the steering vector. In this work, delays were applied prior to computation and application of the weight vector **w**, as is customary in ultrasound adaptive beamforming [32–38]. Delays were updated every 60 samples (0.46 mm) and for every angular step (0.9°).

In the approach implemented in this work, **w** is computed only for sub-apertures of size m=7 with an angular spacing of 0.9° and a rectangular sliding window. The total acquired depth was subdivided into non-overlapping axial segments of n=60 samples (0.46 mm) to compute adaptive weightings that vary through depth. After computation of **R** from acquired data, the windowed sum for a given sub-aperture and axial segment can be computed directly using

$$\boldsymbol{Y}[n]=\mathbf{X}^T\mathbf{w}. \quad (6)$$

Because power minimization techniques are heavily dependent on SNR, diagonal loading is often performed by adding a constant to the diagonal of the covariance matrix (i.e. uncorrelated noise), in order to improve robustness to noise:

$$\mathbf{R}=\mathbf{X}\mathbf{X}^T-\tau\mathbf{I} \quad (7)$$

where **I** is an [$m \times m$] identity matrix and τ is the degree of diagonal loading. Synnevåg et al. reported diagonal loading with τ proportional to the trace of **R** [34], while Vignon and Burcher selected τ based on the eigenvalues of **R** [33]. Adjusting the degree of diagonal loading allows tuning between robustness to electronic noise and rejection of off-axis energy. That is, for heavy diagonal loading, **w** defaults to conventional beamforming, while for low-level diagonal loading, Equation 4 is more susceptible to electronic noise. In this work, we selected $\tau = 0.01 \cdot tr\{\mathbf{X}\mathbf{X}^T\}$, where $tr\{\cdot\}$ is the trace operator, as preliminary simulations indicated that this value of τ ensured robustness while maintaining approximately the same resolution as lighter levels of loading.

2.3 Phase coherence factor processing

In order to increase the CTR in mechanically-steered contrast-enhanced IVUS imaging, signals arising from subsequent acquisitions over several closely-spaced angular positions can be treated as a sub-aperture. This sub-aperture beamsum is **Y**[n] as defined in Equation 6. While minimum variance and related beamformers have demonstrated improved resolution, they also require increased computation and produce images with increased speckle variance relative to the conventional delay-and-sum beamformer [32–38]. An alternative approach to adaptive imaging for the improvement of spatial resolution and contrast is the application of the phase coherence factor (PCF), which operates on beamformed data **Y** rather than on channel data **X**.

The PCF was computed using the phase of delayed radiofrequency (RF) data as previously described [39, 40]. Delays were applied identically to the other processing cases according to Equation 3. Briefly, for every i^{th} depth sample in the axial direction, the phase σ_i was obtained via the analytical signal as described by Camacho et al. [39], as well as the auxiliary phase σ_i^A, in which π was added to σ_i if $\sigma_i < 0$ and -π was added to σ_i if $\sigma_i > 0$ to

avoid phase discontinuities at ± π [40]. The standard deviation of the phase across all received lines in a sub-aperture (in this work, m=7 angular positions) were computed for both σ_i and σ_i^A, where the standard deviation of σ_i is denoted as σ_i and that of σ_i^A, is denoted as σ_i^A. The minimum of σ_i and σ_i^A, denoted σ_{min}, was used in the computation of the phase coherence factor as follows:

$$PCF[n]=1-\frac{\sigma_{\min}}{\sigma_0}, \quad (8)$$

where $\sigma_0=\pi/\sqrt{3}$, the nominal standard deviation for a uniform distribution of phases between −π and +π. In order to allow for tuning of the phase coherence factor, the modified version of PCF was used [39]:

$$PCF^{\gamma}[n]=1-\gamma\frac{\sigma_{\min}}{\sigma_0}, \quad (9)$$

where γ=1 yields increased sidelobe suppression and γ=0 is the non-adaptive case (no PCF weighting).

The phase coherence factor is then applied by using the value of the PCF$^{\gamma}$ to weight the output of the sub-aperture beamsummed data at each depth:

$$\boldsymbol{Y}_{PCF}[n]=PCF^{\gamma}[n]\cdot\boldsymbol{Y}[n]. \quad (10)$$

3. Simulations and experiments

3.1 Simulations

The point spread function (PSF) due to transmitting and receiving with a single element for an ideal point source at a depth of 5 mm was simulated using Field II [45]. Electronic SNR was fixed at 15 dB by adding white Gaussian noise to the received channel signals. Point spread functions were then computed for the cases of no summation, summation with a rectangular window, minimum variance windowing, rectangular windowing with application of the phase coherence factor after beam summation, and minimum variance windowing with application of the phase coherence factor after beam summation (m=7 angular positions with a step size of 0.9°). The diagonal loading parameter τ (Equation 7) was $\tau = 0.01\cdot tr\{\mathbf{X}\mathbf{X}^T\}$ for all minimum variance sums. The PCF control parameter γ was set to 0.25.

In order to assess the performance of minimum variance beamforming and the phase coherence factor in mechanically-steered intravascular ultrasound, intravascular ultrasound images were simulated for each processing case using Field II [45] by positioning a point target at a known location. Transducer properties were matched to the actual transducer, as described in Table 1. Because Field II cannot simulate the nonlinear scattering of tissue or microbubbles (there is no known tool for simulating the superharmonic signal produced by microbubble destruction), pulse-echo simulations at the higher receiving frequency (30

MHz) were used in order to both approximate resolution, which for superharmonic imaging of microbubbles depends primarily on the receiving transducer [28], and to allow analysis of the various processing techniques on background tissue scattering. By using a 30 MHz pulse-echo simulation, we preserve the relationship between the aperture and the wavelength of the propagating wave used in forming the image, ensuring simulated images having similar spatial dimensions and resolution as the dual-frequency IVUS scenario. These simulations differ from the dual-frequency imaging scenario in that the high frequency transmit aperture would be replaced with a low frequency transmit aperture, which would emit a broad beam to excite microbubbles and produce superharmonic signals, yielding an acoustic field full of approximately omnidirectional sources. The use of a pulse-echo approach also allows for evaluation of the proposed processing techniques for B-mode imaging.

The acoustic scattering of the point target was 14 dB greater than the mean scattered amplitude of the background, approximately the CTR previously reported using this transducer [21]. Background scatterers had random scattering amplitude and locations within the field of view and the scatterer density was set to 10 scatterers per resolution cell. 50 simulations were performed for electronic SNRs of 6 dB, 10 dB, 15 dB, and 20 dB, which are similar to those observed *in vivo* for dual-frequency imaging of microbubbles with the described transducer [22]. Contrast was computed for each simulated image using the following equation:

$$\text{Contrast} = 20 \log_{10}\left(\frac{S_{\text{in}} - S_{\text{out}}}{S_{\text{out}}}\right) \quad (11)$$

where S_{in} and S_{out} are the mean pressure signals inside and outside of the target, respectively, at equivalent depths after envelope detection. Lateral resolution was computed for each simulated image at the −6 dB level from the peak of the target after envelope detection but before scan conversion.

3.2 Phantom imaging

Imaging performance was assessed using a custom tissue-mimicking phantom having an attenuation of 0.44 dB/cm/MHz [46]. This phantom was characterized up to 25 MHz after fabrication to measure attenuation and verify the presence of fully-developed speckle at the transmit frequency. The phantom had three straight channels comprised of 200 μm-inner diameter cellulose tubing at depths of 4.0 mm, 4.5 mm, and 7.1 mm. For phantom experiments, lipid-shelled microbubble contrast agents (10^8 microbubbles/mL) were infused through the flow channels at a mean velocity of 17.7 mm/s using a calibrated syringe pump (PHD2000, Harvard Apparatus, Holliston, MA, USA). Radiofrequency data were acquired as the IVUS transducer was pulled through the center of the phantom along a distance of 15.0 mm with step size of 200 μm. Acquired radiofrequency data were digitized at 100 MHz (Signatec PDA14, Corona, CA) and filtered using a 7^{th}-order Butterworth bandpass filter (−6 dB pass band 24.75–30.25 MHz) in Matlab (The Mathworks, Natick, MA). The same processing cases were examined as in simulations: no summation, rectangular windowing, minimum variance windowing, rectangular windowing with application of the phase

coherence factor after beam summation, and minimum variance windowing with application of the phase coherence factor after beam summation. The same PCF tuning parameter (γ = 0.25) and diagonal loading parameter ($\tau = 0.01 \cdot tr\{R\}$) used in the simulations were applied to PCF and MV weightings, respectively, on phantom data. Final images were displayed in Matlab with 30 dB dynamic range to assess tube diameter.

For the simulated images, targets occurred in known locations, however manual target identification was required for phantom data. Manual regions of interest (ROIs) were drawn in each slice using ImageJ (NIH, Bethesda, MD) to assess contrast-to-tissue ratio (CTR) for each type of processing. In order to measure tube diameter, the image was loaded into ImageJ and the tube diameter was determined by drawing a straight line across the target in the lateral (circumferential) direction while displaying only the brightest 6 dB in an image. The observer was not blinded to the data. CTR was computed for each experimentally acquired image using the following equation:

$$CTR = 20 \log_{10}\left(\frac{C}{T}\right) \quad (12)$$

where C and T are the mean pressure signals from regions microbubble contrast agent and tissue, respectively, at equivalent depths and after envelope detection. Improvements in lateral resolution due to applying adaptive windows were evaluated using paired *t*-tests.

3.3 Ex vivo and in vivo imaging

In order to assess the performance of these techniques for imaging *vasa vasorum*, both *ex vivo* and *in vivo* models were utilized. In the *ex vivo* model, mesenteric arteries from Rapacz familial hypercholesterolemic pigs (RFH) [47–49] were used in place of human arteries. These arteries were obtained from the Francis Owens Blood Research Lab (FOBRL, Chapel Hill, NC, USA). RFH pigs are genetically predisposed to develop atherosclerotic lesions which closely mimic the pathology found in humans. RFH pigs have been used previously to evaluate contrast enhancement methods for detecting *vasa vasorum* during the progression of atherosclerosis [50]. Specimens were collected within 24 hours of euthanasia and immediately stored in phosphate buffered saline (PBS) solutions at −20°C until the time of the experiment. After thawing, one specimen was sutured and attached to a custom fixture to allow the vessel to be stretched to the approximate *in vivo* length [51]. A 200 μm-diameter tube was positioned outside the artery to simulate a deep vessel of the *vasa vasorum* and contrast agents were flowed through the vessel at a mean velocity of 88.5 mm/s using the same syringe pump. The artery was submerged in a tank filled with PBS, and both B-mode and dual-frequency mode pullbacks were acquired. All procedures were approved by the University of North Carolina Institutional Animal Care and Use Committee (IACUC).

In addition, we utilized an animal model having vasculature similar in diameter to the vessels of interest (<200 μm), the chorioallantoic membrane (CAM) in chicken embryos. This animal model has been used in several previous contrast-enhanced ultrasound studies and presents a network of vessels having the desired diameter [17, 52–54]. Fertilized chicken eggs (broiler line, Ross 708) were acquired from a local source (North Carolina

State Chicken Educational Unit, Raleigh, NC, USA) and refrigerated at 6°C for 3–7 days until incubation. Eggs were first incubated *in ovo* at 37.5°C with 70% relative humidity for 3 days, turning every 4 hours using an automated egg rocker (Model 4200/3200, Farm Innovators, Plymouth, IN, USA). After 3 days of incubation, eggs were cracked and embryos explanted into disposable holders as described by Schomann, et al. [55]. Embryos were then incubated for 14 days in a humidified incubator at 37.5°C, 70% humidity, and 2.0% CO_2 (NAPCO 8000 Series, Thermo Scientific, Waltham, MA, USA). After growing to day 14 (Hamburger and Hamilton stage 39–40 [56]), two embryos were imaged using the system in Figure 1. The vitelline vein was cannulated to allow the injection of MCAs at a concentration of 10^{10} microbubbles/mL at a mean velocity of 8.8 mm/s using the same syringe pump. This represents a higher concentration relative to those used previously with subharmonic or ultraharmonic imaging [13, 17], although imaging depth, vessel diameter, and type of contrast agent used differ among these studies. The chicken embryo was prepared for imaging by coupling the transducer to the adjacent CAM structure with 37°C PBS. Three-dimensional pullbacks were performed over a distance of 4 mm with a step size of 200 μm. *In vivo* and *ex vivo* data were acquired and processed in the same manner as in the phantom imaging study. Final images were displayed in ImageJ with 30 dB dynamic range.

4. Results

4.1 Simulations

In Figure 2, typical point spread functions (PSFs) are shown for rectangular windowing, MV windowing, rectangular windowing with application of PCF (γ=0.25), and MV windowing with application of PCF. Each PSF is normalized relative to its own peak, and the −6, −10, and −20 dB contours are shown. The −6 dB beam areas are 2.27, 2.45, 2.21, 2.27, and 2.14 mm^2 for no summation, rectangular windowing, MV windowing, rectangular windowing with PCF, and MV windowing with application of PCF, respectively. While summation increases SNR over the non-summed case, any weighting other than rectangular apodization necessarily decreases the beamsummed energy, although it does so with benefit of improved resolution and contrast. The peak levels relative to the no summation case are +10.3 dB for rectangular window, +2.1 dB for MV, +7.5 dB for PCF, and +1.58 dB for MV and PCF.

At these small sub-aperture sizes (m=7 angular positions), improvement due to summation is less than it would be for typical array-based ultrasound imaging, however there is improvement in SNR due to summation alone, with additional reduction in beamwidth (improvement in resolution) due to MV weighting. MV weighting provides clear improvements to the point spread function and beam area relative to other cases, while PCF alone provides reduction in off-axis energy relative to rectangular windowing. Combining MV and PCF improves the resolution (reduces beam area) while still maintaining suppression of off-axis energy.

In Figure 3, illustrative IVUS images from simulation data are shown for each processing case. Each image is normalized to its own maximum and displayed with a dynamic range of 40 dB. Summation with a rectangular window clearly increases the lateral extent of the point target while decreasing the level of the background tissue relative to the point target. When

MV windowing is applied, speckle variance increases, as previously reported with minimum variance beamforming. Application of the phase coherence factor produces images with small but visible improvements in contrast even at γ=0.25, also consistent with previous publications [39, 40]. This improvement in contrast may be due to reduction of off-axis contributions (Figure 2) in a relatively low SNR environment. Note that the theoretical diffraction-limited resolution for this transducer at this depth and frequency is 535 μm.

The lateral resolution and contrast measured across all 50 simulated images at each SNR are summarized in Figures 4 and 5, respectively. While simulated images are displayed with 40 dB of dynamic range in Fig. 3 (display dynamic range in IVUS is typically 17–55 dB [57]), in order to fully display the characteristics of the image, including the background, this dynamic range makes it difficult to visually assess spatial resolution difficult (for example, at the −6 dB level). For this reason, the spatial extent of the target at the −6 dB level is given in Fig. 4 as a standard measurement of resolution. The results observed in simulations with varying values of γ (Figures 4 and 5) are directly applicable to B-mode IVUS processing. Specifically, at γ=0.25 and γ=0.5, PCF processing produces the highest image contrast (Figure 5A–B). Adding PCF to MV processing increases contrast over MV alone. As γ increases, the improvement to image contrast due to PCF processing decreases, where contrast is approximately equal to that of summation alone when γ=0.75 (Figure 5C) and is worse than summation alone when γ=1.0 (Figure 5D). This could be due to PCF processing enhancing relatively bright scatterers which may be randomly positioned at the focus in the “background” region of the image. PCF processing is observed in simulations to impair resolution as the SNR increases, particularly at low values of γ. This is believed to be because there is little energy in the PCF beam at low SNRs, since only 7 channels are summed in this case unlike in the case in which PCF is applied to arrays having many channels.

At γ=0.25, MV processing improves lateral resolution as SNR increases (Figure 4A), providing approximately equivalent lateral resolution relative to the rectangular window case for SNR=10 dB and higher resolution for all SNR values greater than 10 dB. Combining PCF and MV processing ensures higher resolution at the lowest SNR values but otherwise provides similar resolution to MV alone. PCF processing alone provides similar resolution to the summation alone case.

For γ=0.5, PCF processing provides high resolution at low SNR values (Figure 4B). As SNR increases, the lateral resolution increases until it is approximately equal to the case of summation with a rectangular window. Combining MV and PCF ensures high resolution at all SNR values for γ=0.5. For γ=0.75 (Figure 4C), PCF processing further improves lateral resolution and yields improved resolution relative to summation with a rectangular window or no summation for all SNR values. Combining PCF and MV processing at γ=0.75 provides higher resolution than that provided by either PCF or MV alone, particularly at high SNR values. This trend continues for γ=1.0 (Figure 4D), which provides slightly higher resolution than γ=0.5 for both PCF alone and combined MV and PCF processing. However, contrast is low for combined PCF and MV (and any case involving MV) due to the high speckle variance of MV processing.

4.2 Phantom imaging

Illustrative slices through the phantom volume containing the three tubes with microbubble contrast agent are shown in Figure 6. The full view of the acquired IVUS image (with conventional processing, no summation) is displayed in Fig. 6A, while magnified views of the central tube for each processing type are displayed in Fig. 6B–F. CTR and measured tube diameter for every slice in the 15 mm pullback are summarized Figure 7. While summation with a rectangular window was expected to produce inferior lateral resolution to the no summation case (as was observed in simulations), we found similar resolutions at the −6 dB level for these two processing types in phantom testing. This may be due to the reduced contrast in the “no summation” images, as noisy pixels in final “no summation” images may have been included when measuring the target lateral extent. Minimum variance weighting improved resolution by 41.7% at the cost of only a slight decrease in CTR (0.34 dB relative to the rectangular window case). Applying the phase coherence factor alone yields an increase in CTR of 4.2 dB but only a slight improvement in resolution (21.8% relative to the no summation case). Applying both MV and PCF produces improvements in both CTR (4.1 dB) and resolution (41.7%). All improvements in resolution due to application of MV, PCF, or MV and PCF weighting are statistically significant relative to the rectangular window case ($p<0.01$, all cases).

4.3 In vivo imaging

Single slice IVUS images acquired in a 15-day-old chicken embryo are shown for the various types of processing in Figure 8. Vessel diameter and CTR are reported in Table 2 for the two embryos. CTR was computed by measuring the mean pixel brightness in the central vessel (Figures 8 and 9) and also in a region outside the vessel at the same depth. Vessel diameter was measured manually in the same central vessel in ImageJ at the −6 dB level as described in Section 3.2. Both CTR and vessel diameter were measured for every slice which contained the vessel. Measurements were averaged across these slices for each animal. The characteristics observed in simulation and phantom studies persist: any form of summation improves CTR by increasing SNR, while MV windowing improves spatial resolution over non-adaptive windowing at the expense of CTR.

Summation with a rectangular window yields a mean increase in CTR of 3.20 dB relative to no summation, while summation with a rectangular window and PCF produces a nearly identical improvement in CTR of 3.19 dB. While CTR is relatively similar for summation with a rectangular window, rectangular window with PCF, or MV window with PCF, measured vessel diameter decreases with the adaptive processing as the PSF decreases in width as demonstrated in Figure 2. MV windowing, PCF with rectangular windowing, and MV windowing with PCF yielded mean decreases in vessel diameter (i.e. improvement in resolution) of 28.0%, 30.7%, and 37.2%, respectively (Table 2).

4.4 Ex vivo imaging

The results of 3D pullback imaging in the porcine artery are shown in cross sections in Figure 9 and in volume renderings in Figure 10. This image provides a view of the type of data that might be provided by utilizing this imaging approach clinically: B-mode (grayscale) IVUS imaging data providing vessel anatomy (transmit and receive at 30 MHz)

is combined with dual-frequency imaging data (transmit 6.5 MHz, receive 30 MHz, shown in red) providing visualization of the microtube simulating the *vasa vasorum* along the larger excised porcine vessel. The described processing techniques were applied to both the B-mode and dual-frequency data. Summation across m=7 elements visibly enhances the ability to visualize the contrast agent in the 200 μm tube. Images similar to these could prove diagnostically valuable for assessing plaque vulnerability, planning interventional procedures, or for post-procedural monitoring.

5. Discussion

5.1 Simulations

As seen in the PSF simulations (Figure 2), which are normalized to the peak level of each case, applying either MV weighting or the phase coherence factor reduces the sidelobe contributions while maintaining most of the SNR gains due to summation. This result is consistent with the simulated images, in which contrast increases similarly for all summed cases (Figure 5), with resolution also improving in the cases in which MV processing is applied (Figure 4). The resolution improvement due to MV weighting increases with increasing SNR but exists at all SNR levels tested. For the mechanically-steered IVUS imaging scenario explored in this work, additional improvements due to weighted summation might be realized by decreasing angular step size while maintaining the same angular extent in each sub-aperture in order to increase the number of channels in a sum.

The level of diagonal loading employed in the MV processing in this work was the minimum level necessary to ensure improvement in resolution while maintaining robustness for all SNR levels examined (6–20 dB electronic SNR). Further study of the selection of diagonal loading parameter τ is of future interest, particularly the multi-parameter optimization of τ and the PCF parameter γ, which may be of general interest for B-mode IVUS imaging.

In the future, dual-frequency images might be simulated by using tools similar to those used in photoacoustics such as the k-wave toolbox [58]. Because the low frequency beam is used only for exciting microbubbles to produce superharmonic signals, every microbubble within this broad beam would produce a superharmonic signal and could thus be modeled as an omnidirectional acoustic source. As shown in our previous experimental work, resolution depends primarily on the high frequency receiving transducer [28].

5.2 Phantom and *in vivo* imaging experiments

In phantom studies, application of MV weights and the PCF both produced improvements in resolution (Fig. 7A), with all summed cases exhibiting similar CTR (Fig. 7B), as in the simulations when SNR≤ 15 dB (Fig. 5A). This behavior was also observed *in vivo* in the vessels of the chorioallantoic membrane of the two chicken embryos (Table 2), with a 37% improvement in resolution and 2.2 dB improvement in CTR when both MV weighting and PCF were applied. Given the relatively low SNR *in vivo* in the no summation case (14 dB) [21], it is possible that diameter estimation in this case is limited by the SNR, leading to

underestimation. However, the simulation results (Fig. 4) suggest an improvement of 36% at an SNR of 14 dB (Fig. 4A), which is similar to the result in Table 2.

High variances in measurements of CTR in phantom and *in vivo* experiments when either MV or PCF were applied are indicative of the dependence of these processing techniques on SNR, which is consistent with simulations and previous work investigating adaptive beamforming techniques [32–38]. However, the PCF, which was applied only at low levels in the experiments this work ($\gamma = 0.25$) appears to be more robust than adaptive beamforming such as MV in a low-SNR environment. The unique nature of this data, in which echoes originate only from microbubbles with very low-amplitude tissue echoes, must also be considered, as it is quite different from B-mode ultrasound data to which MV and PCF have previously been applied. Specifically, the fully-developed speckle present in B-mode ultrasound images is not expected to be present in these dual-frequency contrast-specific images, though this has not been examined in detail. Acquired *in vivo* images of the fine vasculature in the CAM demonstrate an additional challenge in that some echoes arise from microbubbles in sub-resolution vessels, making these regions appear noisy when they are actually filled with microbubbles in vessels that are still too small to resolve in spite of the described improvements. This effect has previously been accounted for *in vivo* using a metric known as volumetric vascular density [59].

Additionally, because the underlying nature of the data is different between simulations (B-mode) and experimental data (dual-frequency broadband superharmonic), there are observed differences in image contrast. The primary performance limitation of the transducer is its SNR, so although the SNR was varied within realistic ranges for the simulations, the acquired dual-frequency data acquired with this transducer typically has CTR (i.e. contrast) which is limited by SNR rather than by the amplitudes of the physical signals produced by the contrast and the tissue [22].

In quantifying observed improvements in the phantom images presented in this article, (Figure 7), we are able to measure vessel diameters closer to 200 μm when using adaptive processing techniques (i.e. 282 μm for 200 μm tubes, Figure 7B). We have also observed modest improvements to both contrast-to-tissue ratio and the ability to measure vessel diameters *in vivo* in a chicken embryo model (Figure 8, Table 2), which is encouraging for high resolution IVUS imaging in an *in vivo* environment such as for *vasa vasorum* imaging.

5.3 Considerations for implementation and implications for *vasa vasorum* imaging

In this article we have demonstrated the potential benefits to both image contrast and spatial resolution due to applying two adaptive processing techniques to contrast-enhanced IVUS imaging. These benefits occur with the same hardware and acquisition parameters that we have previously used with this prototype system. However, as all processing presented in this work was performed offline, a potential challenge exists in implementing these techniques in real-time. In the initial paper describing the application of the phase coherence factor in ultrasound, Camacho et al. discuss in detail the efficient implementation of this technique [39], suggesting that PCF may be able to be implemented in a commercial IVUS system. Implementing adaptive beamforming may be more difficult and costly, though several near-

real time implementations of adaptive beamformers with large array-based systems have recently been demonstrated [60–63].

Another consideration for this particular technique, which utilizes superharmonic echoes from partial destruction of microbubbles [42], is the frame rate, which needs to be kept sufficiently low to allow microbubble reperfusion. While IVUS imaging in general strives to maintain higher rotation rates to allow for averaging and high frame rates, decreased rotation rates which are necessary to allow for microbubble reperfusion also provide increased computation time. For reduced rotation rate IVUS such as for superharmonic microbubble imaging, sub-aperture beamforming could provide an alternative means of improving SNR and contrast given that averaging across multiple revolutions may be impractical due to the influence of motion artifacts at these lower rates. For IVUS in general, the techniques presented in this article could be applied by saving RF data (i.e. during a single pullback) and reconstructing afterwards to yield a higher resolution image. For B-mode IVUS, averaging signals acquired from the same angular positions could be used to improve SNR while maintaining constant resolution, although the adaptive signal processing techniques presented in this article have also demonstrated improved resolution relative to the no summation case in simulations of B-mode IVUS images (Figure 4).

In this article, we have described signal processing approaches which allow formation of images in which a 200 μm tube measures 282 μm using a prototype dual-frequency transducer. We have also demonstrated the ability to image 200–300 μm vessels in an animal model, with the proposed processing yielding a mean decrease in vessel diameter of 37.2%. Further improvements in resolution may be realized by the development of new transducer prototypes. The reported improvements in resolution may also be helpful in other applications of intravascular ultrasound such as peripheral vascular disease or in endoscopic ultrasound.

6. Conclusions

In this work, we have applied sub-aperture beamforming to data acquired using a prototype mechanically-steered IVUS transducer at adjacent angular locations. Specifically, conventional and minimum variance beamforming were applied to sub-apertures of seven elements, and the phase coherence factor was applied after summation. These approaches were demonstrated in tissue-mimicking phantoms, an *ex vivo* porcine artery, and *in vivo* using a chicken embryo model. In phantom studies, PCF processing improved CTR by a mean of 4.2 dB, while combining PCF and MV processing decreased spatial resolution by 41.7%. Combining both techniques demonstrated preservation of both benefits, with mean improvements of 2.2 dB in contrast and 37.2% in resolution observed *in vivo*. Additional gains may potentially be realized in the future by optimizing selection of tuning parameters for these adaptive techniques to better match the SNR. Applying these processing strategies can enhance image quality in IVUS, a low-SNR imaging technique where resolution is at a premium.

Acknowledgments

The authors wish to thank Tim Nichols, M.D. for providing the porcine artery. This work was supported by grants R01EB015508 and F32EB018715 from the National Institutes of Health and by pilot funding from North Carolina State University's Chancellor's Innovation Fund.

References

1. World Health Organization. Fact sheet no. 310: The top 10 causes of death. 2014 May. 2014
2. Mintz GS, Nissen SE, Anderson WD, Bailey SR, Erbel R, Fitzgerald PJ, et al. American College of Cardiology Clinical Expert Consensus Document on Standards for Acquisition, Measurement and Reporting of Intravascular Ultrasound Studies (IVUS). A report of the American College of Cardiology Task Force on Clinical Expert Consensus Documents. J Am Coll Cardiol. 2001 Apr. 37:1478–1492. [PubMed: 11300468]
3. Maehara A, Mintz GS, Weissman NJ. Advances in intravascular imaging. Circ Cardiovasc Interv. 2009 Oct.2:482–490. [PubMed: 20031760]
4. Falk E. Why Do Plaques Rupture. Circulation. 1992 Dec.86:30–42.
5. Finn AV, Nakano M, Narula J, Kolodgie FD, Virmani R. Concept of vulnerable/unstable plaque. Arterioscler Thromb Vasc Biol. 2010 Jul.30:1282–1292. [PubMed: 20554950]
6. Nair A, Kuban BD, Tuzcu EM, Schoenhagen P, Nissen SE, Vince DG. Coronary plaque classification with intravascular ultrasound radiofrequency data analysis. Circulation. 2002 Oct 22.106:2200–2206. [PubMed: 12390948]
7. Kawasaki M, Takatsu H, Noda T, Sano K, Ito Y, Hayakawa K, et al. In vivo quantitative tissue characterization of human coronary arterial plaques by use of integrated backscatter intravascular ultrasound and comparison with angioscopic findings. Circulation. 2002 May 28.105:2487–2492. [PubMed: 12034654]
8. Kawasaki M, Sano K, Okubo M, Yokoyama H, Ito Y, Murata I, et al. Volumetric quantitative analysis of tissue characteristics of coronary plaques after statin therapy using three-dimensional integrated backscatter intravascular ultrasound. Journal of the American College of Cardiology. 2005 Jun 21.45:1946–1953. [PubMed: 15963391]
9. de Korte CL, Pasterkamp G, van der Steen AF, Woutman HA, Bom N. Characterization of plaque components with intravascular ultrasound elastography in human femoral and coronary arteries in vitro. Circulation. 2000 Aug 8.102:617–623. [PubMed: 10931800]
10. Tearney GJ, Regar E, Akasaka T, Adriaenssens T, Barlis P, Bezerra HG, et al. Consensus standards for acquisition, measurement, and reporting of intravascular optical coherence tomography studies: a report from the International Working Group for Intravascular Optical Coherence Tomography Standardization and Validation. J Am Coll Cardiol. 2012 Mar 20.59:1058–1072. [PubMed: 22421299]
11. Sethuraman S, Aglyamov SR, Amirian JH, Smalling RW, Emelianov SY. Intravascular photoacoustic imaging using an IVUS imaging catheter. Ieee Transactions on Ultrasonics Ferroelectrics and Frequency Control. 2007 May.54:978–986.
12. Jansen K, van der Steen AFW, van Beusekom HMM, Oosterhuis JW, van Soest G. Intravascular photoacoustic imaging of human coronary atherosclerosis. Optics Letters. 2011 Mar 1.36:597–599. [PubMed: 21368919]
13. Goertz DE, Frijlink ME, Tempel D, Bhagwandas V, Gisolf A, Krams R, et al. Subharmonic contrast intravascular ultrasound for vasa vasorum imaging. Ultrasound Med Biol. 2007 Dec. 33:1859–1872. [PubMed: 17683850]
14. Maresca D, Renaud G, van Soest G, Li X, Zhou Q, Shung KK, et al. Contrast-enhanced intravascular ultrasound pulse sequences for bandwidth-limited transducers. Ultrasound Med Biol. 2013 Apr.39:706–713. [PubMed: 23384459]
15. Goertz DE, Frijlink ME, de Jong N, van der Steen AF. Nonlinear intravascular ultrasound contrast imaging. Ultrasound Med Biol. 2006 Apr.32:491–502. [PubMed: 16616596]

16. Goertz DE, Frijlink ME, Tempel D, van Damme LC, Krams R, Schaar JA, et al. Contrast harmonic intravascular ultrasound: a feasibility study for vasa vasorum imaging. Invest Radiol. 2006 Aug. 41:631–638. [PubMed: 16829746]
17. Maresca D, Skachkov I, Renaud G, Jansen K, van Soest G, de Jong N, et al. Imaging microvasculature with contrast-enhanced ultraharmonic ultrasound. Ultrasound Med Biol. 2014 Jun.40:1318–1328. [PubMed: 24613639]
18. Yu FT, Villanueva FS, Chen X. Radial modulation contrast imaging using a 20-MHz single-element intravascular ultrasound catheter. IEEE Trans Ultrason Ferroelectr Freq Control. 2014 May.61:779–791. [PubMed: 24803134]
19. Kwon HM, Sangiorgi G, Ritman EL, Lerman A, McKenna C, Virmani R, et al. Adventitial vasa vasorum in balloon-injured coronary arteries: visualization and quantitation by a microscopic three-dimensional computed tomography technique. J Am Coll Cardiol. 1998 Dec.32:2072–2079. [PubMed: 9857895]
20. Doinikov AA, Haac JF, Dayton PA. Resonance frequencies of lipid-shelled microbubbles in the regime of nonlinear oscillations. Ultrasonics. 2009 Feb.49:263–268. [PubMed: 18977009]
21. Ma J, Martin K, Dayton PA, Jiang X. A preliminary engineering design of intravascular dual-frequency transducers for contrast-enhanced acoustic angiography and molecular imaging. IEEE Trans Ultrason Ferroelectr Freq Control. 2014 May.61:870–880. [PubMed: 24801226]
22. Martin KH, Lindsey BD, Ma J, Nichols TC, Jiang X, Dayton PA. Intravascular Contrast Specific Imaging of Microvessels Using a Dual-Frequency Approach. 2015 *in review*.
23. Martin KH, Lindsey BD, Ma J, Lee M, Li S, Foster FS, et al. Dual-Frequency Piezoelectric Transducers for Contrast Enhanced Ultrasound Imaging. Sensors (Basel). 2014; 14:20825–20842. [PubMed: 25375755]
24. Kim J, Li SB, Kasoji S, Dayton PA, Jiang XN. Dual-frequency Super Harmonic Imaging Piezoelectric Transducers for Transrectal Ultrasound. Health Monitoring of Structural and Biological Systems 2015. 2015; 9438
25. Qiu WB, Chen Y, Wong CM, Liu BQ, Dai JY, Zheng HR. A novel dual-frequency imaging method for intravascular ultrasound applications. Ultrasonics. 2015 Mar.57:31–35. [PubMed: 25454093]
26. Ma JG, Martin KH, Li Y, Dayton PA, Shung KK, Zhou QF, et al. Design factors of intravascular dual frequency transducers for super-harmonic contrast imaging and acoustic angiography. Physics in Medicine and Biology. 2015 May 7.60:3441–3457. [PubMed: 25856384]
27. Guiroy A, Novell A, Ringgaard E, Lou-Moeller R, Gregoire JM, Abellard AP, et al. Dual-frequency transducer for nonlinear contrast agent imaging. IEEE Trans Ultrason Ferroelectr Freq Control. 2013 Dec.60:2634–2644. [PubMed: 24297028]
28. Lindsey BD, Rojas JD, Martin KH, Shelton SE, Dayton PA. Acoustic characterization of contrast-to-tissue ratio and axial resolution for dual-frequency contrast-specific acoustic angiography imaging. IEEE Trans Ultrason Ferroelectr Freq Control. 2014 Oct.61:1668–1687. [PubMed: 25265176]
29. Lindsey BD, Shelton SE, Dayton PA. Optimization of contrast-to-tissue ratio through pulse windowing in dual-frequency "acoustic angiography" imaging. Ultrasound Med Biol. 2015 Jul. 41:1884–1895. 2015. [PubMed: 25819467]
30. Gessner RC, Aylward SR, Dayton PA. Mapping microvasculature with acoustic angiography yields quantifiable differences between healthy and tumor-bearing tissue volumes in a rodent model. Radiology. 2012 Sep.264:733–740. [PubMed: 22771882]
31. Shelton SE, Lee YZ, Foster FS, Lee M, Cherin E, Aylward SR, et al. Quantification of microvascular tortuosity during tumor evolution utilizing acoustic angiography. Ultrasound Med Biol. 2015; 41:1896–1904. [PubMed: 25858001]
32. Mann, JA.; Walker, WF. A constrained adaptive beamformer for medical ultrasound: Initial results; 2002 Ieee Ultrasonics Symposium Proceedings, Vols 1 and 2; 2002. p. 1807-1810.
33. Vignon F, Burcher MR. Capon beamforming in medical ultrasound imaging with focused beams. Ieee Transactions on Ultrasonics Ferroelectrics and Frequency Control. 2008 Mar.55:619–628.
34. Synnevag JF, Austeng A, Holm S. Benefits of Minimum-Variance Beamforming in Medical Ultrasound Imaging. Ieee Transactions on Ultrasonics Ferroelectrics and Frequency Control. 2009 Sep.56:1868–1879.

35. Asl BM, Mahloojifar A. Contrast Enhancement and Robustness Improvement of Adaptive Ultrasound Imaging Using Forward-Backward Minimum Variance Beamforming. Ieee Transactions on Ultrasonics Ferroelectrics and Frequency Control. 2011 Apr.58:858–867.
36. Asl BM, Mahloojifar A. A Low-Complexity Adaptive Beamformer for Ultrasound Imaging Using Structured Covariance Matrix. Ieee Transactions on Ultrasonics Ferroelectrics and Frequency Control. 2012 Apr.59:660–667.
37. Asl BM, Mahloojifar A. Minimum Variance Beamforming Combined with Adaptive Coherence Weighting Applied to Medical Ultrasound Imaging. Ieee Transactions on Ultrasonics Ferroelectrics and Frequency Control. 2009 Sep.56:1923–1931.
38. Holfort IK, Gran F, Jensen JA. Broadband Minimum Variance Beamforming for Ultrasound Imaging. Ieee Transactions on Ultrasonics Ferroelectrics and Frequency Control. 2009 Feb. 56:314–325.
39. Camacho J, Parrilla M, Fritsch C. Phase coherence imaging. IEEE Trans Ultrason Ferroelectr Freq Control. 2009 May.56:958–974. [PubMed: 19473914]
40. Hasegawa H, Kanai H. Effect of subaperture beamforming on phase coherence imaging. IEEE Trans Ultrason Ferroelectr Freq Control. 2014 Nov.61:1779–1790. [PubMed: 25389157]
41. Given CA, Attizzani GF, Jones MR, Ramsey CN, Brooks WH, Costa MA, et al. Frequency-Domain Optical Coherence Tomography Assessment of Human Carotid Atherosclerosis Using Saline Flush for Blood Clearance without Balloon Occlusion. American Journal of Neuroradiology. 2013 Jul.34:1414–1418. [PubMed: 23391841]
42. Lindsey BD, Rojas JD, Dayton PA. On the relationship between microbubble fragmentation, deflation, and broadband superharmonic signal production. Ultrasound Med Biol. 2015 Jun. 41:1711–1725. 2015. [PubMed: 25766572]
43. Tremblay-Darveau C, Williams R, Milot L, Bruce M, Burns PN. Combined Perfusion and Doppler Imaging Using Plane-Wave Nonlinear Detection and Microbubble Contrast Agents. Ieee Transactions on Ultrasonics Ferroelectrics and Frequency Control. 2014 Dec.61:1988–2000.
44. Capon J. High-Resolution Frequency-Wavenumber Spectrum Analysis. Proceedings of the Ieee. 1969; 57:1408-&.
45. Jensen JA, Svendsen NB. Calculation of Pressure Fields from Arbitrarily Shaped, Apodized, and Excited Ultrasound Transducers. Ieee Transactions on Ultrasonics Ferroelectrics and Frequency Control. 1992 Mar.39:262–267.
46. Madsen EL, Zagzebski JA, Banjavie RA, Jutila RE. Tissue mimicking materials for ultrasound phantoms. Med Phys. 1978 Sep-Oct;5:391–394. [PubMed: 713972]
47. Hasler-Rapacz J, Ellegren H, Fridolfsson AK, Kirkpatrick B, Kirk S, Andersson L, et al. Identification of a mutation in the low density lipoprotein receptor gene associated with recessive familial hypercholesterolaemia in swine. American Journal of Medical Genetics. 1998 Apr 13.76:379–386. [PubMed: 9556295]
48. Grunwald KAA, Schueler K, Uelmen PJ, Lipton BA, Kaiser M, Buhman K, et al. Identification of a novel Arg ->Cys mutation in the LDL receptor that contributes to spontaneous hypercholesterolemia in pigs. Journal of Lipid Research. 1999 Mar.40:475–485. [PubMed: 10064736]
49. Hasler-Rapacz JO, Nichols TC, Griggs TR, Bellinger DA, Rapacz J. Familial and Diet-Induced Hypercholesterolemia in Swine - Lipid, Apo-B, and Apoa-I Concentrations and Distributions in Plasma and Lipoprotein Subfractions. Arteriosclerosis and Thrombosis. 1994 Jun.14:923–930. [PubMed: 8199183]
50. Schinkel AFL, Krueger CG, Tellez A, Granada JF, Reed JD, Hall A, et al. Contrast-enhanced ultrasound for imaging vasa vasorum: comparison with histopathology in a swine model of atherosclerosis. European Journal of Echocardiography. 2010 Sep.11:659–664. [PubMed: 20385655]
51. Han HC, Ku DN. Contractile responses in arteries subjected to hypertensive pressure in seven-day organ culture. Annals of Biomedical Engineering. 2001 Jun.29:467–475. [PubMed: 11459340]
52. Stieger SM, Caskey CF, Adamson RH, Qin S, Curry FR, Wisner ER, et al. Enhancement of vascular permeability with low-frequency contrast-enhanced ultrasound in the chorioallantoic membrane model. Radiology. 2007 Apr.243:112–121. [PubMed: 17392250]

53. Schellpfeffer MA, Kolesari GL. Microbubble contrast imaging of the cardiovascular system of the chick embyro. Ultrasound Med Biol. 2012 Mar.38:504–510. [PubMed: 22266227]
54. Faez T, Skachkov I, Versluis M, Kooiman K, de Jong N. In vivo characterization of ultrasound contrast agents: microbubble spectroscopy in a chicken embryo. Ultrasound Med Biol. 2012 Sep. 38:1608–1617. [PubMed: 22766113]
55. Schomann T, Qunneis F, Widera D, Kaltschmidt C, Kaltschmidt B. Improved method for ex ovo-cultivation of developing chicken embryos for human stem cell xenografts. Stem cells international. 2013; 960958:1–9.
56. Hamburger V, Hamilton HL. A Series of Normal Stages in the Development of the Chick Embryo. Journal of Morphology. 1951; 88:49-&. [PubMed: 24539719]
57. Tsakanikas VD, Fotiadis DI, Michalis LK, Naka KK, Bourantas CV. Intravascular Imaging: Current Applications and Research Developments. Intravascular Imaging: Current Applications and Research Developments. 2012:1–456.
58. Treeby BE, Cox BT. k-Wave: MATLAB toolbox for the simulation and reconstruction of photoacoustic wave fields. J Biomed Opt. 2010 Mar-Apr;15:021314. [PubMed: 20459236]
59. Dunleavey JM, Xiao L, Thompson J, Kim MM, Shields JM, Shelton SE, et al. Vascular channels formed by subpopulations of PECAM1+ melanoma cells. Nat Commun. 2014; 5:5200. [PubMed: 25335460]
60. Kim, K.; Park, S.; Park, S-C.; Kang, J.; Kim, Y-T.; Kim, J-H. Fast transform-based adaptive beamformer for medical ultrasound imaging; Image Processing (ICIP), 2013 20th IEEE International Conference on; Melbourne, Australia. 2013. p. 2329-2333.
61. Szasz, T.; Basarab, A.; Vaida, M-F.; Kouame, D. IEEE International Ultrasonics Symposium. Chicago, IL, USA: 2014. Beamforming with sparse prior in ultrasound medical imaging; p. 1077-1080.
62. Chen, JY.; Yiu, BYS.; So, HKH.; Yu, ACH. Real-Time GPU-Based Adaptive Beamformer for High Quality Ultrasound Imaging; 2011 Ieee International Ultrasonics Symposium (Ius); 2012. p. 474-477.
63. Asen JP, Buskenes JI, Nilsen CIC, Austeng A, Holm S. Implementing capon beamforming on a GPU for real-time cardiac ultrasound imaging. IEEE Trans Ultrason Ferroelectr Freq Control. 2014 Jan.61:76–85. 2014. [PubMed: 24402897]

Highlights

- Methods for improving spatial resolution and sensitivity in intravascular ultrasound (IVUS) imaging are proposed.
- The two approaches are based on minimum variance (MV) beamforming and the phase coherence factor (PCF).
- The efficacy of the approaches is evaluated in simulations and in experiments with tissue-mimicking phantoms, *ex vivo* porcine arteries, and chicken embryos (*in vivo*).
- In contrast-enhanced IVUS, improvements in both contrast-to-tissue ratio and spatial resolution can be achieved by appropriate application of the proposed techniques.

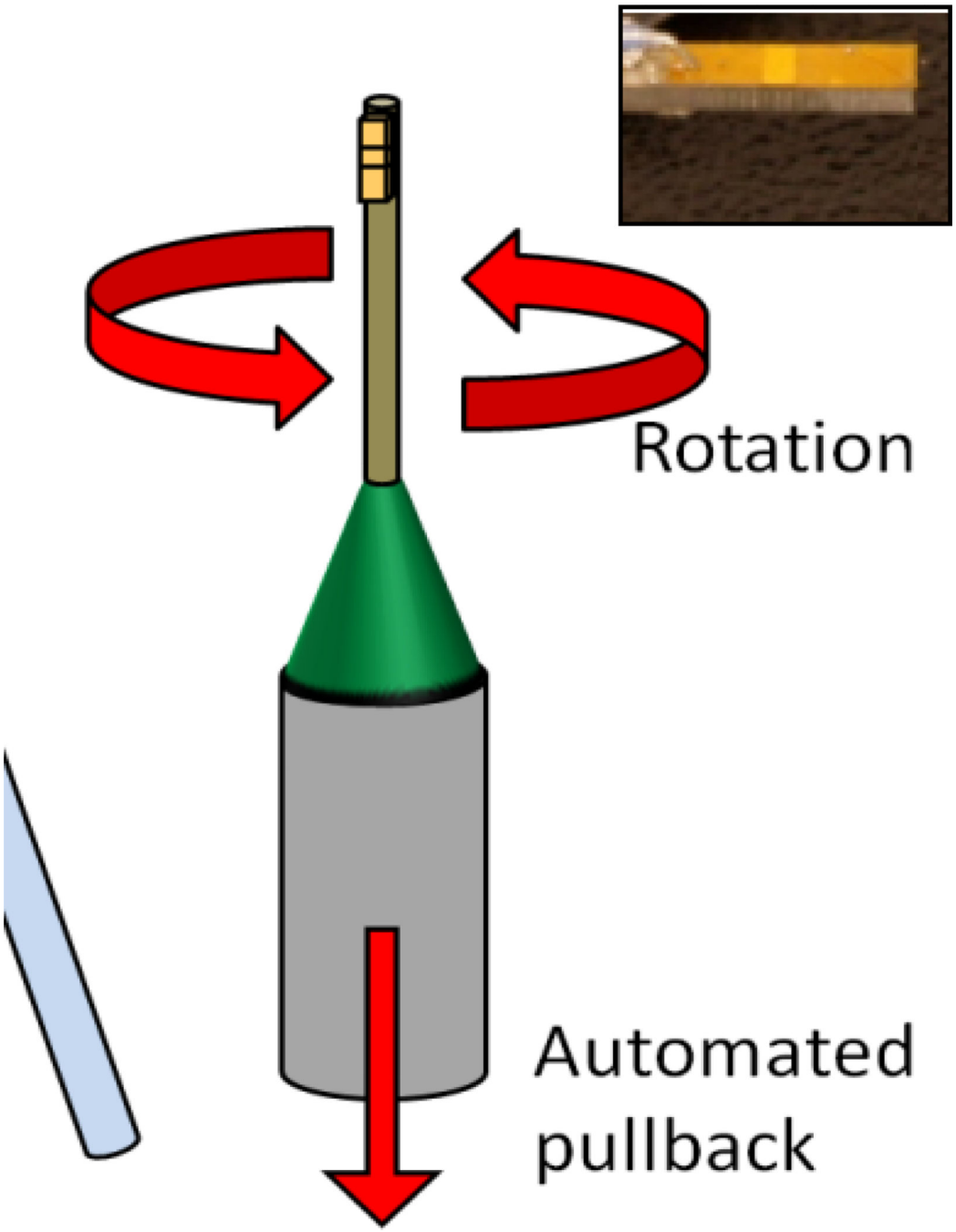

Figure 1.

Diagram of dual-frequency mechanically-steered transducer and (inset)) photograph of prototype transducer used in this study. The lighter central region is the receive element, which is positioned in front of longer transmit element. The total length of the transmit element is 3 mm.

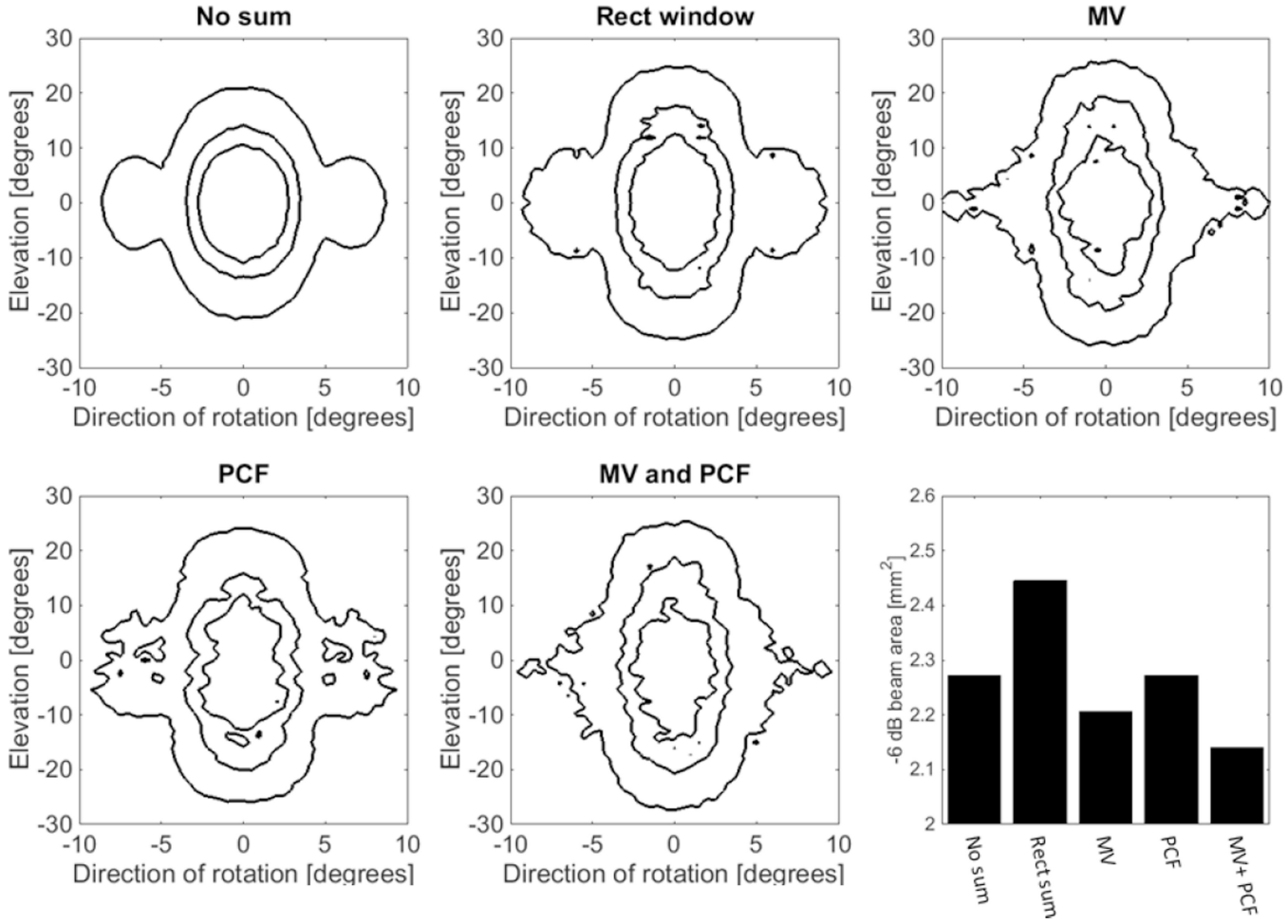

Figure 2.

Contours of PSFs at −6 dB, −10 dB, and −20 dB are shown for processing with no summation, summation with a rectangular window, MV window, rectangular window and PCF, and MV window and PCF, all with 15 dB of SNR at 0.5 cm depth. Each PSF is normalized to its own peak. −6 dB beam areas (bottom right) are given for each PSF. The central of 7 acquisitions occurs at 0°.

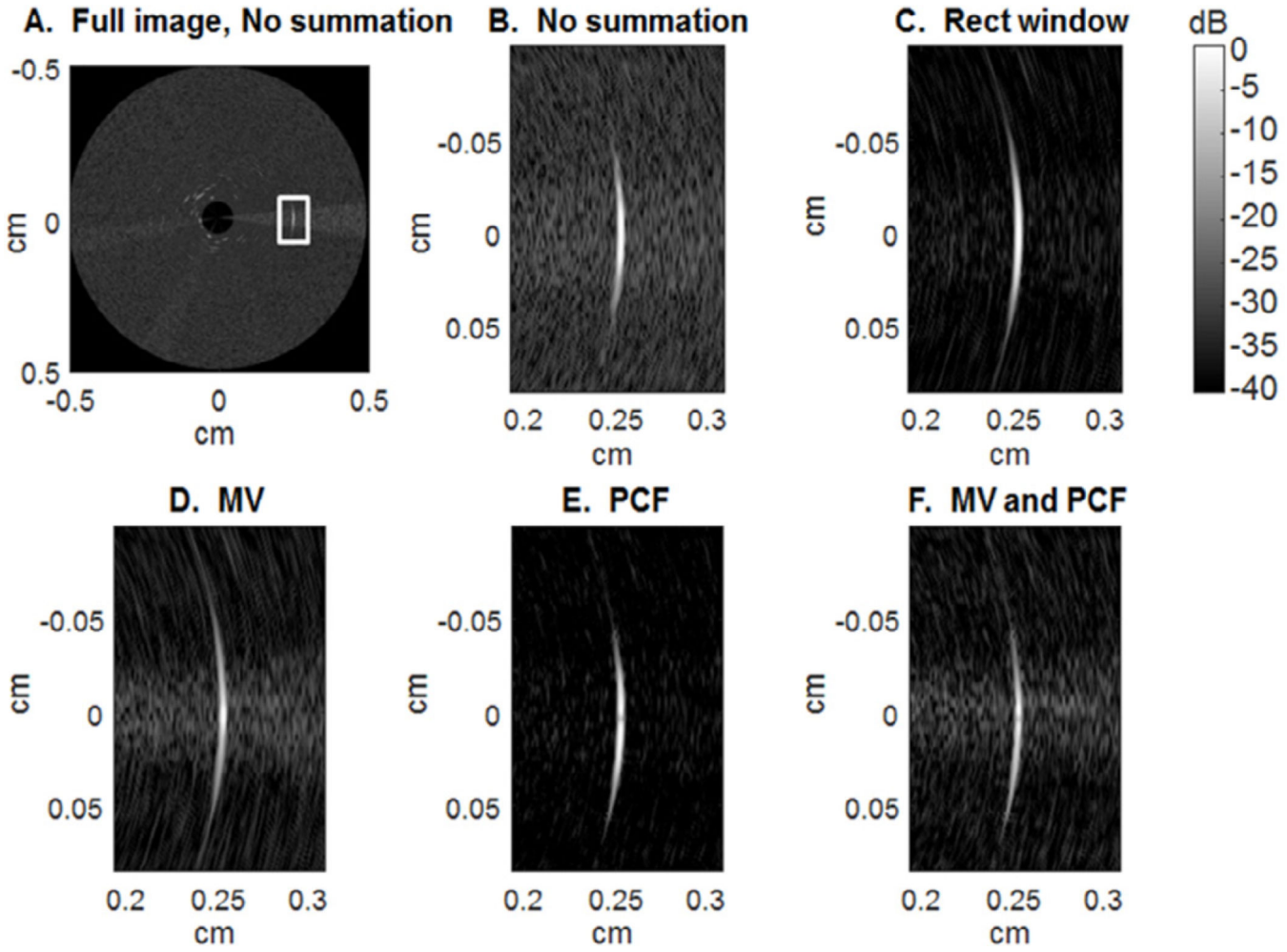

Figure 3.

Example image simulated using Field II with a single point target at a depth of 5 mm (SNR=15 dB). All images are displayed on the same scale with a dynamic range of 40 dB. Entire simulated image with conventional processing (region of interest indicated by the white box) and magnified views of the point target with (B) conventional processing (no summation), (C) Summation with a rectangular window, (D) Summation with a minimum variance window, (E) Summation with a rectangular window and application of the phase coherence factor, and (F) Summation with a minimum variance window and application of the phase coherence factor.

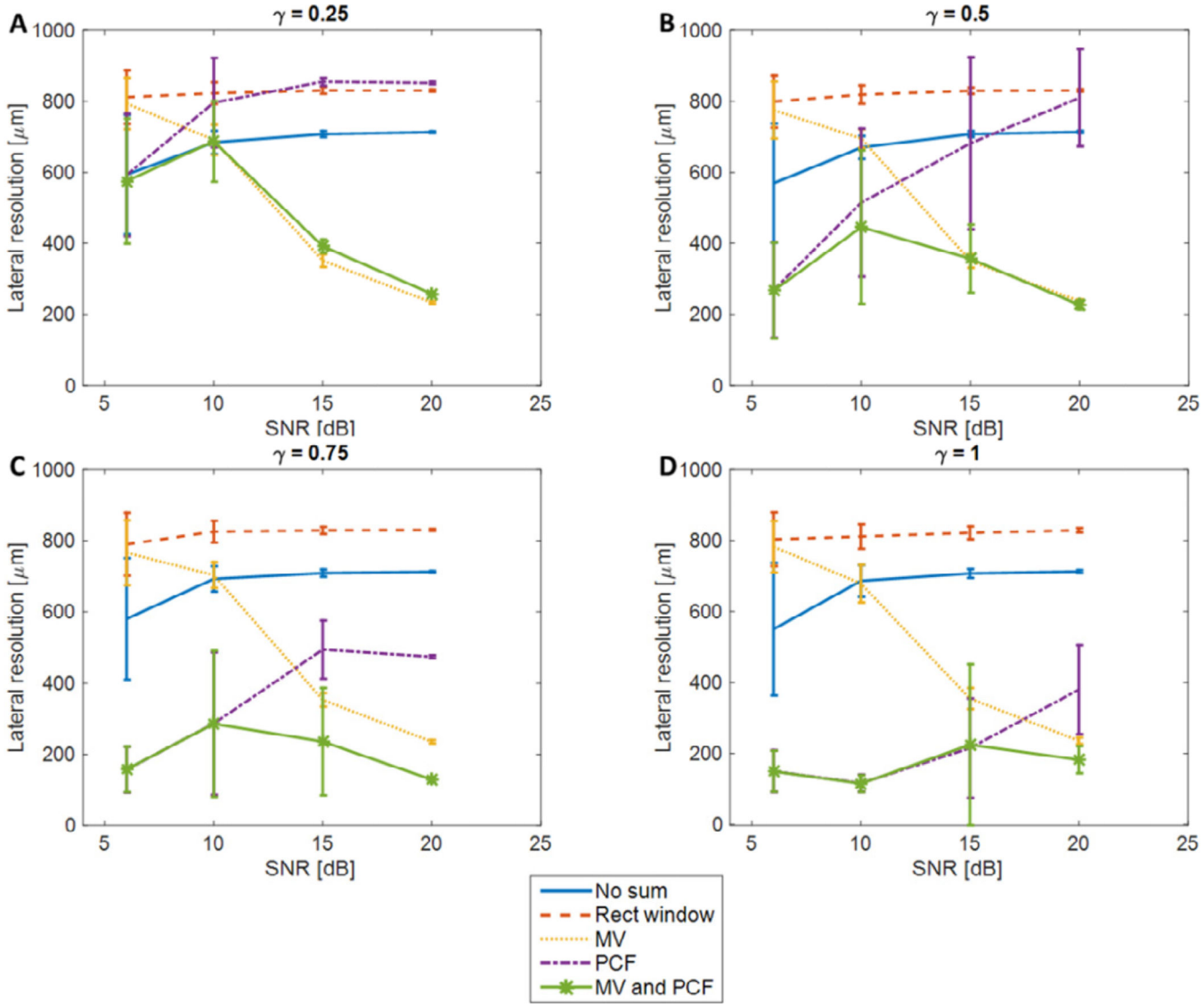

Figure 4.

Simulated lateral resolution as a function of SNR for 4 different values of PCF tuning parameter γ. (A) γ = 0.25, (B) γ = 0.50, (C) γ = 0.75, and (D) γ =1.0. Lateral resolution is determined by measuring the lateral extent of a sub-resolution point target as in Figure 1. The theoretical diffraction-limited resolution λz/D = 535 μm at f_0 = 28 MHz, z = 5 mm, D = 0.5 mm. Each point represents 50 simulations.

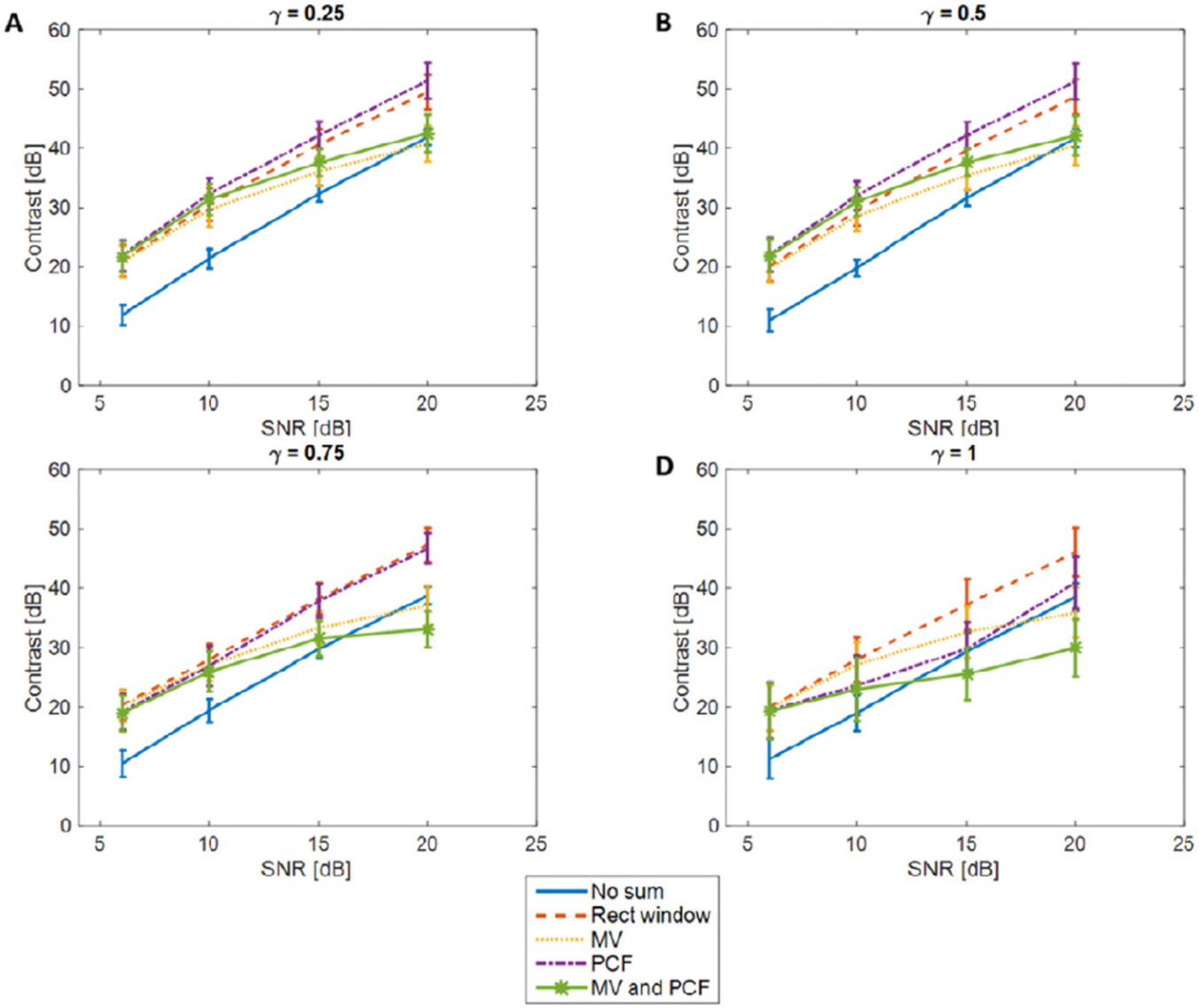

Figure 5.

Simulated image contrast as a function of SNR for 4 different values of PCF tuning parameter γ. (A) γ = 0.25, (B) γ = 0.50, (C) γ = 0.75, and (D) γ =1.0. Contrast is determined by applying Equation 11 within a region containing a known target and at a second region at an equivalent depth.

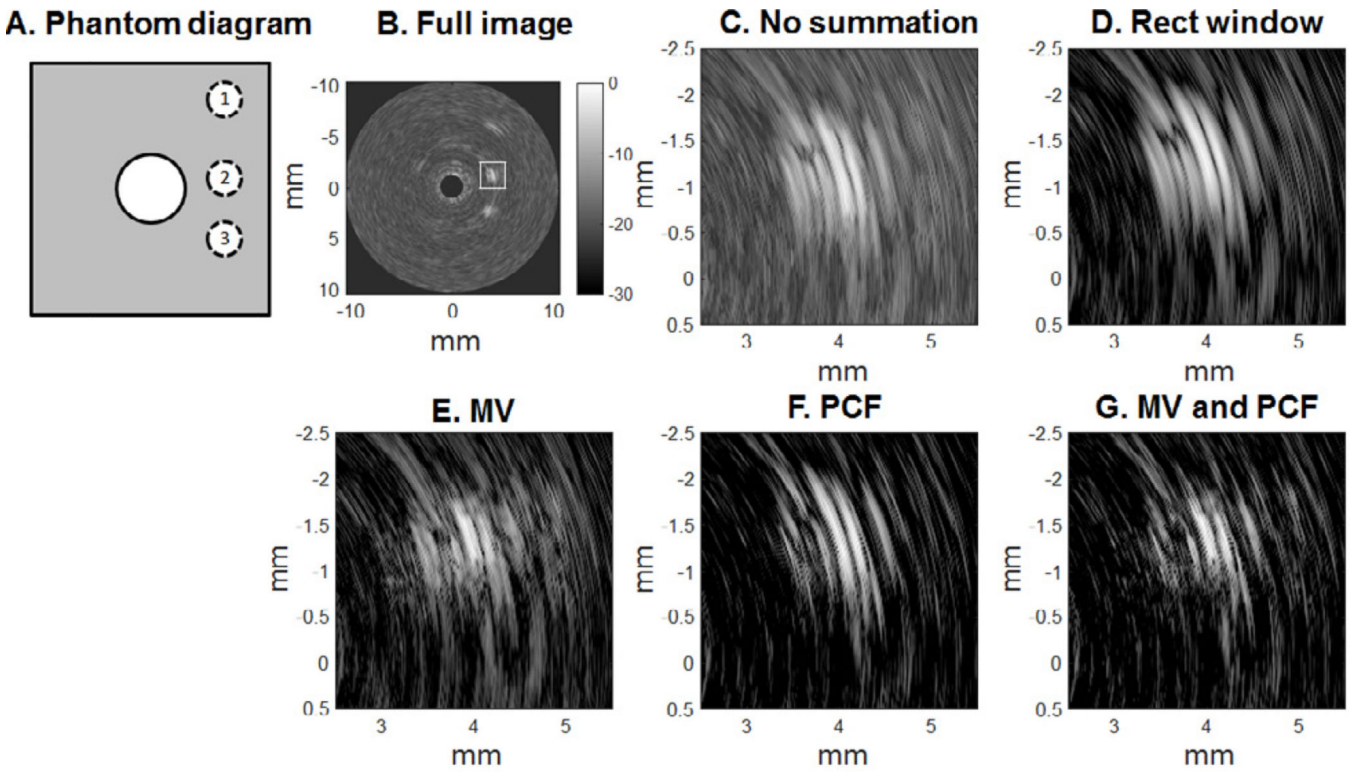

Figure 6.

Illustrative slices through the center of the tissue-mimicking phantom (A) with three parallel tubes filled with microbubble contrast agent at distances of (1) 7.1 mm, (2) 4.5 mm, and (3) 4.1 mm. (B) Full image view (no summation) indicating the region of interest, and magnified views of the center tube with (C) no summation, (D) summation with a rectangular window, (E) MV window, (F) rectangular window with PCF, and (G) MV window with PCF.

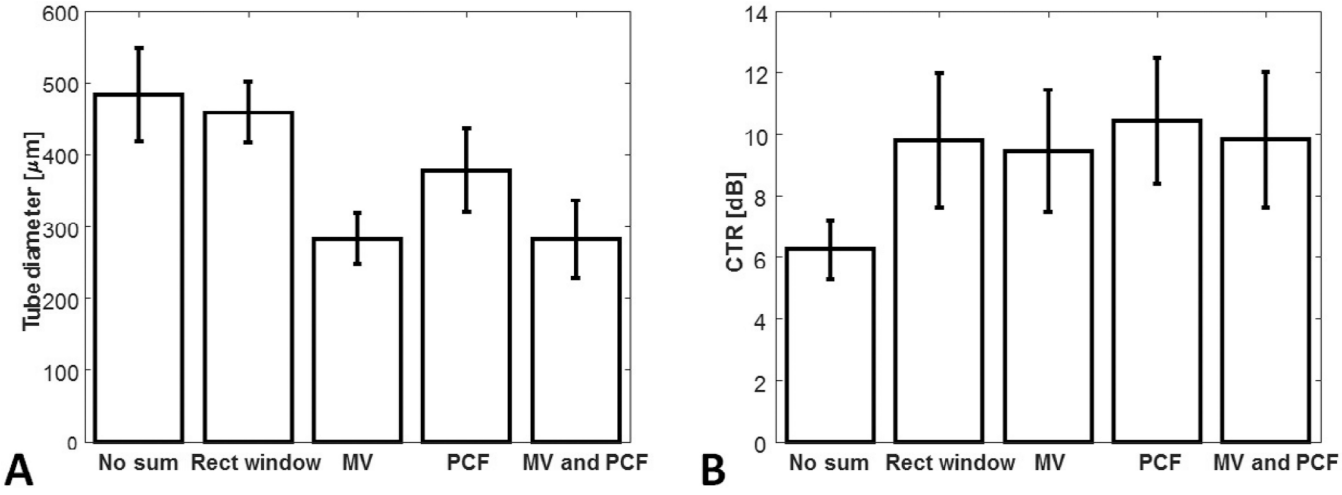

Figure 7.

(A) Mean vessel diameter in a tissue mimicking phantom (Figure 6) as a function of processing type across all slices in the acquired 3D phantom pullback. Improvements in resolution due to application of MV, PCF, and MV+PCF weighting are statistically significant relative to the rectangular window case ($p<0.01$ in all cases). (B) Contrast-to-tissue ratio as a function of processing type across all slices in the acquired 3D phantom pullback.

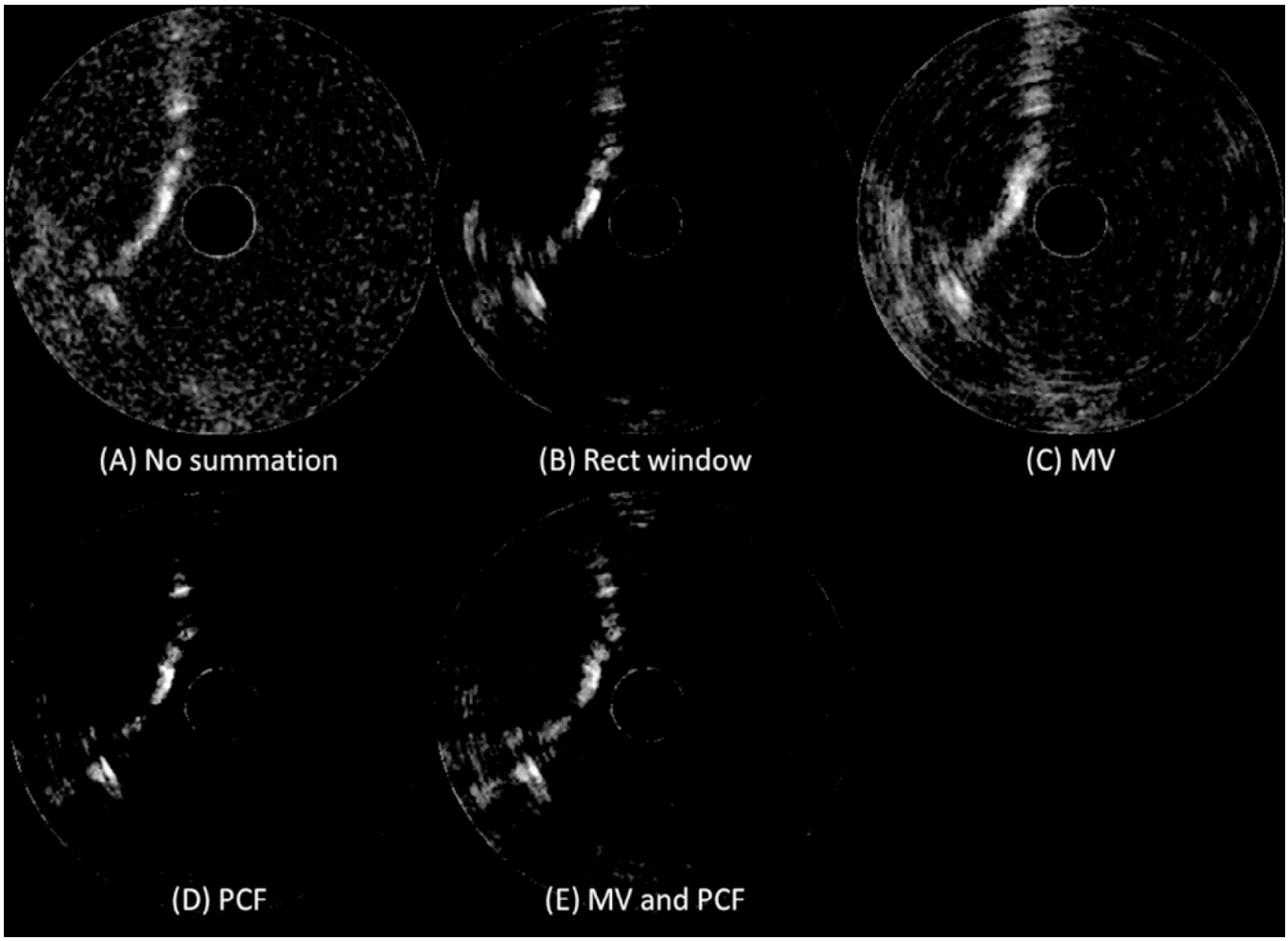

Figure 8.

In vivo slices through vessels of the chorioallantoic membrane in a 15-day-old chicken embryo with (A) no summation, (B) rectangular window, (C) minimum variance window, (D) rectangular window and phase coherence factor, and (E) minimum variance window and phase coherence factor. Scale bar indicates 1 mm.

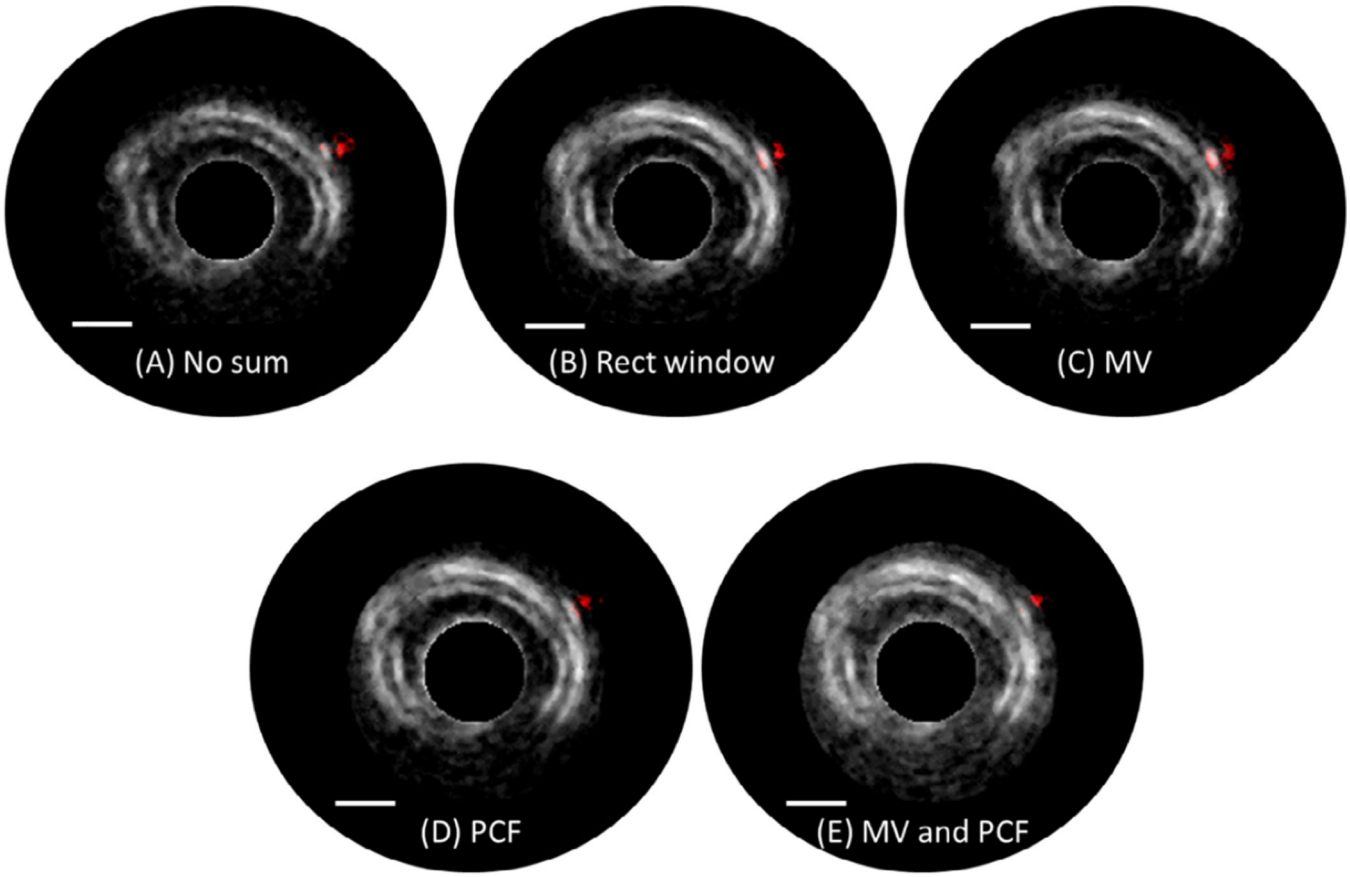

Figure 9.

Cross-section views of ex vivo porcine arteries (grayscale) and an adjacent tube filled with microbubble contrast agent (red) positioned outside of the vessel to mimic *vasa vasorum*. Scale bar indicates 1 mm.

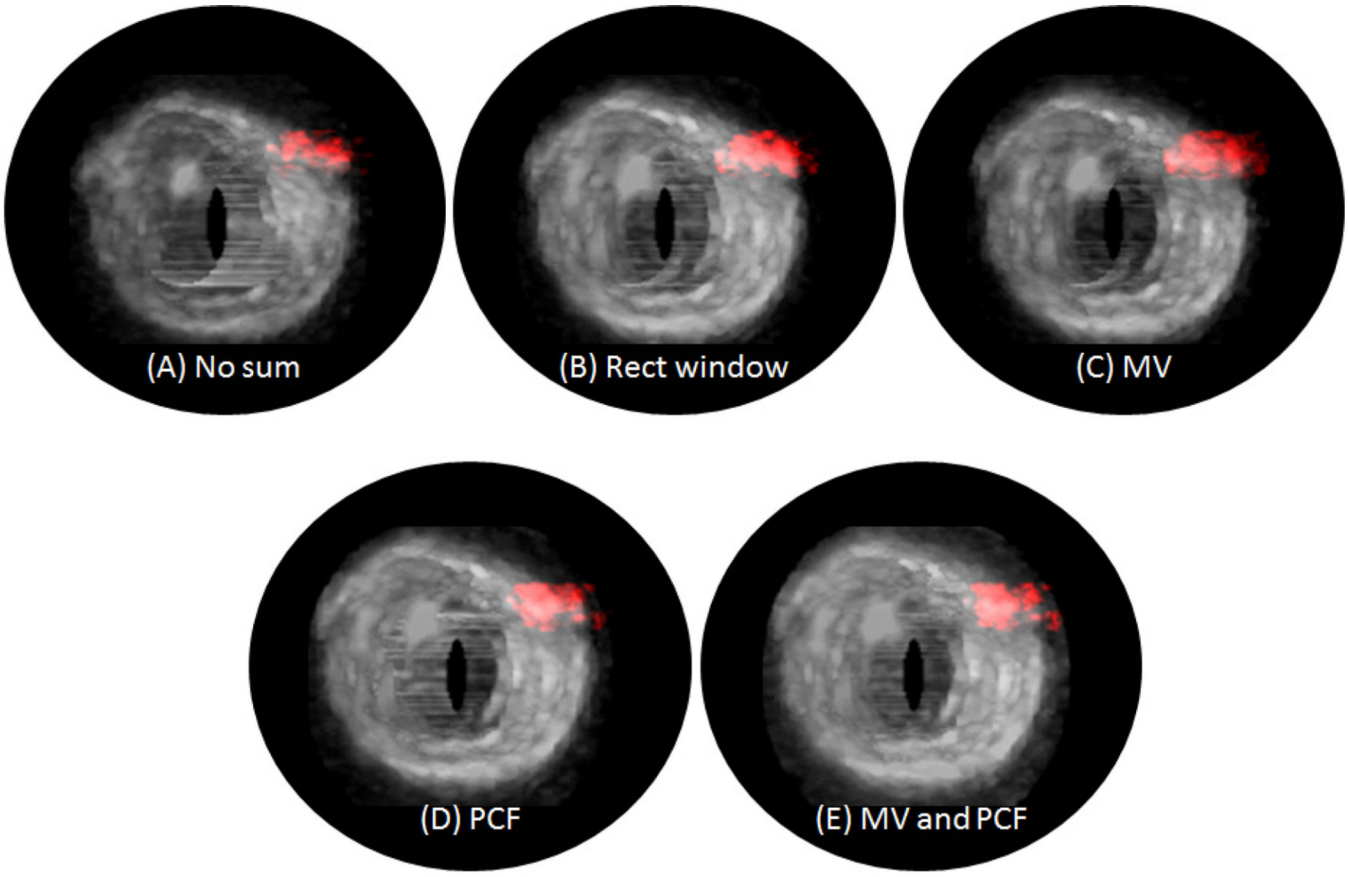

Figure 10.

3D renderings of imaging data acquired via motorized pullback in a porcine artery with a tube filled with microbubble contrast agent positioned outside of the vessel to mimic *vasa vasorum*.

Table 1

Characteristics of the prototype transducer used in this work.

Parameter	Transmit element	Receive element
Center frequency (MHz)	6.5	30
−6 dB bandwidtth	20%	59%
Thickness (μm)	300	65
Width (mm)	0.6	0.6
Length (mm)	3	0.5

Table 2

CTR and vessel diameter measured across all relevant slices in two 15-day-old chicken embryos.

	CTR [dB]			Vessel Diameter [μm]		
	Embryo 1	**Embryo 2**	**Mean change**	**Embryo 1**	**Embryo 2**	**Mean change**
No summation	10.8 ± 2.4	12.0 ± 1.5	-	430.9 ± 102.2	484.9 ± 62.2	-
Rect window	13.9 ± 2.8	15.3 ± 1.0	+3.2 dB	394.5 ± 104.1	353.8 ± 55.6	−17.7%
MV window	11.0 ± 2.8	12.5 ± 1.1	+0.3 dB	363.9 ± 71.6	288.6 ± 77.2	−28.0%
PCF	13.5 ± 2.7	15.7 ± 0.8	+3.2 dB	372.6 ± 109.1	253.2 ± 33.0	−30.7%
MV and PCF	11.7 ± 2.7	15.5 ± 0.8	+2.2 dB	323.6 ± 115.2	244.6 ± 32.5	−37.2%